Energy deposition by nonequilibrium charge states of MeV ^{127}I in Au

Petter Ström[*] and Daniel Primetzhofer

Applied Nuclear Physics, Department of Physics and Astronomy,Uppsala University, Box 516, SE-751 20 Uppsala, Sweden

The energy loss of iodine ions at initial charge states up to 25+ and energies up to 36 MeV in self-supporting gold foils between 37 and 107 nm of thickness was measured with an electron mirror type time-of-flight detector. An excess energy loss of 130 keV was observed at 36 MeV for charge state 25+ compared to 16+, and an energy loss deficit of 100 keV was observed for charge state 8+. The charge state equilibration length for 36-MeV iodine was estimated to lie between 3 and 7 nm, corresponding to an equilibration time between 0.4 and 0.9 fs. This result is relevant both for nanostructure fabrication with MeV ion beams and for depth profiling based on ion beam analysis data in cases where the charge state of the primary ion is far from the equilibrium value in the sample under study. A comparison to published data on charge state equilibration for various projectile-target combinations and energies from 10 keV to 6 GeV indicated that the energy scaling of the equilibration length observed at high energy is invalid for projectile velocities on the order of the Bohr velocity and below. The measurement further provided equilibrium values of the electronic stopping power for iodine in gold at ten energies between 10 and 36 MeV.

I. INTRODUCTION

Studies of the energy loss experienced by energetic ions as they traverse matter are relevant both from a fundamental perspective as they permit us to obtain knowledge about ion-solid interactions, and for applications as they provide input data for quantitative ion beam analysis or allow us to predict the response of a material to irradiation [1–4]. The stopping power dE/dx, i.e., the energy loss per unit path length, is known to show a dependence on the projectile charge state [5], and is expected to scale with the projectile charge as Z_1^2 [6,7]. An ion impinging on a target in an initial charge state different from the average value eventually established as a result of electron exchange with the material thus exhibits a modified energy deposition during the charge state equilibration. At low ion velocities, i.e., approximately up to the Bohr velocity v_0 ($\approx 2.19 \times 10^6$ m/s), this effect has to be accounted for in modeling of dE/dx for ions heavier than protons [8] despite the equilibrium charge state being close to 0, as experiments show characteristic effects of charge exchange on dE/dx even for simple systems such as He [9]. Increased energy loss with increasing charge state has been observed, for example for 140 keV N, and the implications for low to medium energy ion implantation have been discussed [10–12]. For heavy ions in the MeV range, apparently, the magnitude of the deviation

from the equilibrium value of dE/dx can even exceed the equilibrium value itself. It has further been shown for 24-MeV C and 64-MeV S projectiles impinging on a C target that full charge state equilibration takes place over a layer thickness of a few tens to more than $100 \, \mu g/cm^2$, i.e., up to several hundred nm [13,14]. The equilibration length increases with increasing projectile velocity. For example, approximately $700 \, \mu g/cm^2$ of C($\approx 3 \, \mu m$) is required to equilibrate $^{132}Xe^{44+}$ at a specific energy of 43.9 MeV/nucleon [15].

Understanding the characteristics of charge state equilibration for heavy ions is of importance for the expected modification of a target material under irradiation. The total energy deposited near the sample surface is affected by out-of-equilibrium stopping as well as the potential energy released when repopulating vacant projectile electron states. The latter is particularly important at low energies [16], whereas the former is expected to yield a more pronounced effect for energies at which a significant path length is traversed before charge state equilibrium is established. Various nanostructures may be formed during irradiation [17], and since the geometries of these structures depend on dE/dx, they may be modified by varying the charge state [18]. Nanopores mimicking the properties of channels in biological membranes are here of particular interest [19,20]. Furthermore, depth profiling of elemental fractions in a sample using time-of-flight elastic recoil detection analysis (ToF-ERDA) with a heavy ion beam at glancing incidence has been stated to yield a surface depth resolution as good as 2 nm for a 23-MeV $^{127}I^{6+}$ beam impinging on a Cu sample [21]. In a case where the primary ions are far out of charge state equilibrium the modification of the stopping power may affect depth perception on a similar scale, possibly introducing artifacts in the deduced composition profiles. Even when primary ions are close to the equilibrium charge state, a similar effect might occur after a

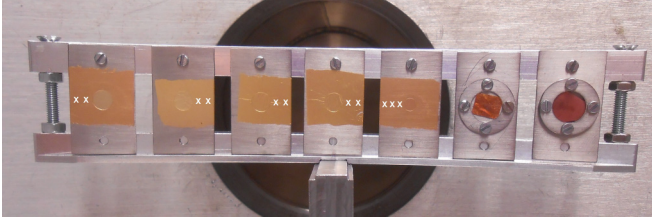*Corresponding author: petter.strom@physics.uu.se

FIG. 1. Au foils mounted on sample holder in measurement chamber. White x's indicate approximate points at which the foil thickness was measured with RBS.

scattering or recoil event as the charge states immediately after a collision are far from equilibrium. ERDA with monolayer surface resolution using a magnetic spectrograph for recoil detection has been demonstrated for a 60-MeV $^{127}I^{23+}$ beam and detection of $^{12}C^{5+}$ recoils [22,23]. In order to maximize the energy loss to energy spread ratio the use of highly charged projectiles was essential for these studies.

While direct studies of the nonequilibrium stopping power in the MeV regime are scarce, the energy deposition of 60-MeV ^{58}Ni in C foils for initial charge states between 8+ and 16+ has been previously examined and a difference within a range of almost 60 keV was observed [24,25]. To improve our understanding of the effects discussed above and provide additional data on charge state dependent energy loss with a maximum charge state further from the expected equilibrium in the target [26] we studied, with a similar practical approach, energy deposition by ions of ^{127}I in Au foils. Conclusions on characteristic equilibration lengths and times are drawn based on the deviation from equilibrium energy loss, a comprehensive comparison with data obtained in previous studies is carried out and the scaling of the equilibration time with projectile velocity and charge state is investigated.

II. EXPERIMENT

A beam of highly charged ions was prepared in the 5-MV pelletron tandem accelerator at Uppsala University by introducing a thin carbon stripping foil before the analyzing magnet in which charge-state–energy combinations of interest were selected. Energies up to 36 MeV and charge states between 3+ and 25+ were applied in this work. The selected ions were transmitted through self-supporting Au foils of thicknesses from 2.2×10^{17} to 6.3×10^{17} at./cm^2 (approximately 37–107 nm assuming the bulk density of 19.30 g/cm^3 for Au), which are shown mounted on a sample holder in Fig. 1. Foil thicknesses and impurity fractions were measured with Rutherford backscattering spectrometry (RBS) and time-of-flight elastic recoil detection analysis (ToF-ERDA) [27]. RBS measurements were performed in two to three points on each sample, indicated in Fig. 1, to ensure foil homogeneity. Transmitted ions of all exit charge states were detected after the Au foils in a time-of-flight system with electron mirror timing detectors (EMTDs) [28]. Signals pertaining to different exit charge states are thus added to produce the data considered below. The energy loss experienced in the foil was obtained as the difference between the energy calculated from the measured flight time peak and the value selected in the
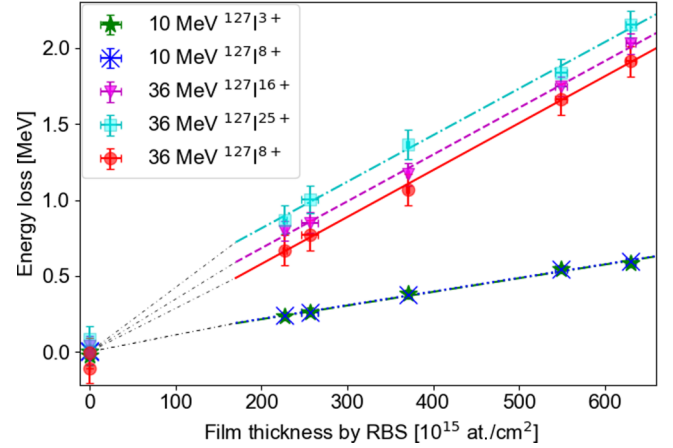

FIG. 2. Energy loss of 10- and 36-MeV ^{127}I in Au foil as a function of foil thickness for different initial charge states. The lines present at foil thicknesses larger than 1.7×10^{17} at./cm^2 are fits to the respective data sets, and the fine dash-dotted extensions of these lines down to 0 foil thickness suggest a modified stopping power during charge state equilibration. Note that a slightly larger drift between the two data points obtained without Au foil at the start and end of each measurement sequence was observed during the measurement with charge state 8+ at 36 MeV than with 16+ and 25+. The drift is discussed further in the Appendix.

analyzing magnet. Further details pertaining to foil production, foil characterization, beam preparation, and energy loss measurements are given in the Appendix.

III. RESULTS

The measured energy loss is reported as a function of impurity compensated Au foil thickness in Fig. 2. The uncertainty in foil thickness is obtained from the difference between the individual measurement points on each sample, while possible errors in energy loss contain three components: (i) the estimated fit error for the peak position, (ii) the drift of the ToF calibration measured as the difference in peak position for measurements without Au foil at the start and end of the run, and (iii) the error in ion energy estimated from the error in the analyzing magnet field. See the Appendix for an extended analysis of potential error sources.

Several features of the graphs in Fig. 2 are of interest. First, the slopes of the lines fit to the measured data are independent of charge state and give the electronic stopping power for transmitted ions (assuming bulk atomic density in the foil) after charge state equilibration. Second, the offset between the lines for charge states 8+, 16+, and 25+ at 36 MeV corresponds to the difference in cumulative energy loss during charge state equilibration; an excess energy loss of approximately 130 keV is thus observed for charge state 25+ compared to 16+, and an energy loss deficit of approximately 100 keV is observed for charge state 8+. Third, as an energy loss offset is measured, but this offset does not vary with foil thickness, the charge state equilibration length must be smaller than the thickness of the thinnest foil. A smaller offset than that between the lines fit to the 36-MeV data is noted for the data points at 0 foil thickness, i.e., without any Au
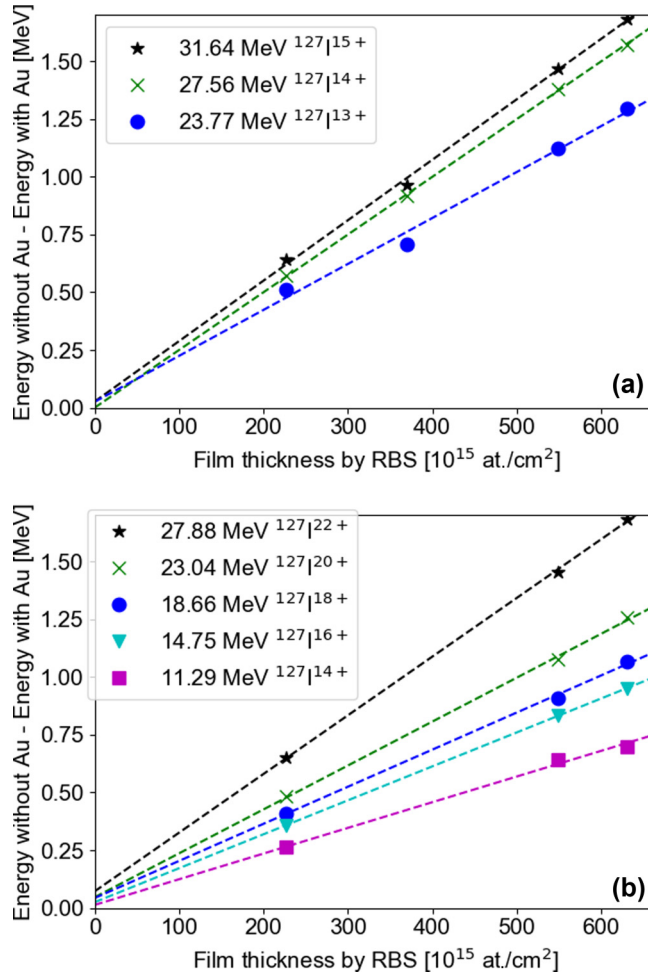
FIG. 3. Energy loss for additional charge state/energy combinations produced when selecting operating conditions to yield (a) 36-MeV ^{127}I^{16+}, (b) 36-MeV ^{127}I^{25+}.

foil present. This is due to the energy loss experienced during charge state equilibration in the C foil of the first EMTD, which only occurs in the case where ions reach the EMTD without first passing through Au.

Charge-state–energy combinations other than those explicitly intended, which reached the foil and detector setup when the C stripping foil was used, gave rise to additional flight time peaks from which further energy loss data could be extracted (see Fig. 8 and related discussion in the Appendix). This energy loss is given as a function of foil thickness with lines fit to each dataset in Figs. 3(a) and 3(b). Table I gives the slopes (equilibrium electronic stopping power in transmission geometry) of all lines in Figs. 2 and 3 and electronic stopping powers at the same initial energies from SRIM2013 [29]. We

note that the fit lines in Fig. 3(b) display a trend of increasing vertical offset with increasing charge state. This is indicative of charge state dependent stopping in the Au foil which is larger than that in the first EMTD foil, but as different charge states are not available at the same energy in this case we make no attempt to perform a quantitative comparison. Our measured electronic stopping powers are slightly larger than those from SRIM2013, and similar to the data obtained by Kantre *et al.* [30] for energies above 20 MeV. Below 20 MeV, the present values are lower than those by Kantre, possibly due to the fact that our measurements were performed in transmission. As trajectories of particles reaching the detector in this geometry exclude close range interactions with target nuclei, the energy loss is decreased. In other words, the mean charge state in large angle scattering geometries is expected to be elevated compared to transmission with a small acceptance angle, leading to consequently increased electronic energy loss out of charge state equilibrium. We note that the maximum deflection angle in a single collision which allows an ion passing the Au foil to hit the second EMTD foil in our setup is approximately 0.5°, corresponding to a closest approach distance between projectile and target nucleus of 0.2 Å at 10 MeV. In comparison, the 45° scattering in [30] yields a closest approach of 0.01 Å, accompanied by a shift of outgoing ions towards higher charge states immediately after the collision as well as additional inelastic energy loss in the collision.

IV. DISCUSSION

In order to assign further meaning to our measured energy loss offsets from Fig. 2, we adopt a simple model for the variation of the projectile charge state q with depth in the target. Assuming, as proposed by Bohr and Lindhard [31], that the initial charge state on average approaches the equilibrium value as

$$q = q_{\mathrm{eq}} + (q_{\mathrm{in}} - q_{\mathrm{eq}})e^{-x/d}, \qquad (1)$$

where q_{in} and q_{eq} are the initial and equilibrium charge states in units of the elementary charge, x is the depth in the target, and d is the characteristic length over which the difference between the actual and equilibrium projectile charge states is reduced by a factor e^{-1} (referred to below as "equilibration length"), the stopping power will be

$$\frac{dE}{dx} = \left(\frac{dE}{dx}\right)_{\mathrm{eq}} \left(\frac{q}{q_{\mathrm{eq}}}\right)^2$$

$$= \left(\frac{dE}{dx}\right)_{\mathrm{eq}} \left[1 + 2\left(\frac{q_{\mathrm{in}}}{q_{\mathrm{eq}}} - 1\right)e^{-x/d} + \left(\frac{q_{\mathrm{in}}}{q_{\mathrm{eq}}} - 1\right)^2 e^{-2x/d}\right].$$

$$(2)$$

TABLE I. Equilibrium electronic stopping powers measured at ten energies between 10 and 36 MeV compared to electronic stopping powers from SRIM2013.

Energy (MeV)	36.00	31.64	27.88	27.56	23.77	23.04	18.66	14.75	11.29	10.00
Electronic stopping [eV/(10^{15} at./cm^2)]	3078[a]	2617	2540	2498	1989	1901	1606	1469	1112	900[a]
SRIM [eV/(10^{15} at./cm^2)]	2786	2508	2252	2230	1952	1897	1552	1228	939	834

[a]Obtained as the average slope from measurements with different initial charge states.

It is assumed here that the equilibration length is short enough that the equilibrium stopping power, $(dE/dx)_{eq}$, is not modified over the depth range of interest, and that stopping scales with the projectile charge state squared. Thus, the energy loss experienced until depth x_f is given by

$$
\Delta E = \int_0^{x_f} \frac{dE}{dx}dx
$$
$$
= \left(\frac{dE}{dx}\right)_{eq}\left[x - 2d\left(\frac{q_{in}}{q_{eq}} - 1\right)e^{-x/d}\right.
$$
$$
\left. - \frac{1}{2}d\left(\frac{q_{in}}{q_{eq}} - 1\right)^2 e^{-2x/d}\right]_0^{x_f}.
\tag{3}
$$

Removing the linear dependence on x_f related to equilibrium stopping, the excess energy loss is

$$
\Delta E_{ex}(x_f) = d\left(\frac{dE}{dx}\right)_{eq}\left[2\left(\frac{q_{in}}{q_{eq}} - 1\right)\left(1 - e^{-x_f/d}\right)\right.
$$
$$
\left. + \frac{1}{2}\left(\frac{q_{in}}{q_{eq}} - 1\right)^2\left(1 - e^{-2x_f/d}\right)\right],
\tag{4}
$$

which letting x_f approach infinity yields the observed offset:

$$
\Delta E_{ex}(x_f \to \infty) = d\left(\frac{dE}{dx}\right)_{eq}\left[2\left(\frac{q_{in}}{q_{eq}} - 1\right) + \frac{1}{2}\left(\frac{q_{in}}{q_{eq}} - 1\right)^2\right].
\tag{5}
$$

The equilibration length for a given energy loss excess or deficit can thus be extracted. With equilibrium electronic stopping 18.17 keV/nm (converted from our measured slope provided in Table I) for 36-MeV I in Au, and excess energy loss 130 keV for $q_{in} = 25$, $q_{eq} = 16.8$ (from the formula for solid state target in [26]), the value of d is 6.5 nm. Similarly, a deficit of 100 keV for $q_{in} = 8$ yields $d \approx 6.0$ nm. The corresponding equilibration times t_{eq} are approximately 0.9 and 0.8 fs.

Using charge state 16+ instead of the presumed equilibrium value 16.8+ when measuring the energy loss offsets in Au at 36 MeV yields with an equilibration length of 6 nm an error of approximately 10 keV by (5), resulting in 8–10% errors in the estimated equilibration lengths (in addition to the errors due to drift and analyzing magnet field discussed in the Appendix). Indeed, selecting 17+ might yield a more realistic representation of the equilibrium as it allows the stripped ion to have the electron configuration of Kr. On the other hand, the line fit to the data for charge state 16+ acquired with Au foil in Fig. 2 actually exhibits a positive offset of approximately 67 keV, i.e., an excess energy loss compared to the case without Au foil where charge state dependent stopping only occurs in the first EMTD C foil. This would seem to indicate either that the actual equilibrium charge state is lower than 16+ or that there is an additional energy loss associated with passing through the Au foil even in the case where its thickness approaches 0 and the incoming charge state is equal to the equilibrium value. Comparing our results to the ones in Refs. [24,25], for 60-MeV ^{58}Ni^{18+} [equilibrium charge state 13.3+, equilibrium electronic stopping (SRIM2013): 8.94 keV/nm], an excess energy loss of 22.8 keV yields an equilibration length of 3.3 nm (0.75 μg/cm^2) and
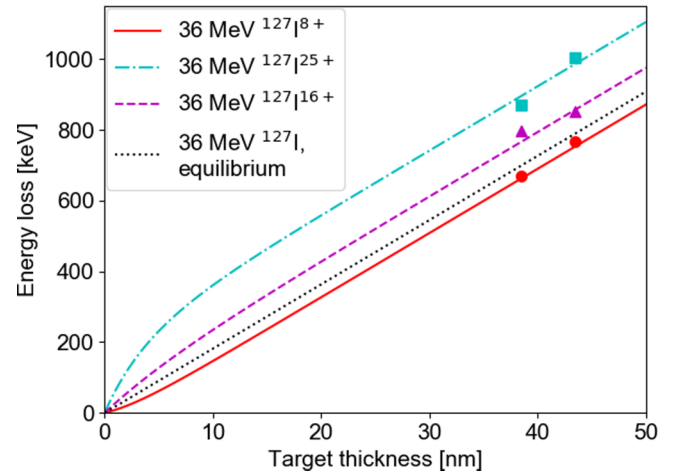

FIG. 4. Energy loss of 36-MeV ^{127}I in Au calculated as per (3) with equilibrium charge state 12.7+, equilibrium stopping 18.17 keV/nm, and equilibration lengths 3 nm for charge state 8+, 6.7 nm for 16+, and 4.5 nm for 25+. Measurement points for the two thinnest Au foils are shown for comparison.

a deficit of 35.7 keV for ^{58}Ni^{8+} yields 5.6 nm (1.3 μg/cm^2). This is in approximate agreement with the directly observed equilibration lengths in Fig. 2 of [24], and corresponds to an equilibration time of 0.2–0.4 fs. The equilibrium charge state in this case was assumed to be the one for which the energy loss offset would be 0 in Table 1 of [25], which is lower than the value of 16.6+ calculated as per Ref. [26]. Thus, the observation that there is a positive energy loss offset at the expected equilibrium charge state by the formula for solid target in [26] is made both in the present work and in [25].

Since the calculated equilibration times depend on the estimated value of the equilibrium charge state, we use Bohr's simple formula by Eq.(4.4.1) in [32] as a second estimate for our data. This yields an equilibrium charge state for 36-MeV ^{127}I of 12.7+, and we have the observed 67-keV excess energy loss for charge state 16+, 197 keV for 25+, and a deficit of 37 keV for 8+. Inserting these in (5) gives equilibration lengths of 6.7, 4.5, and 3.0 nm, with equilibration times 0.9, 0.6, and 0.4 fs, respectively. With our two possible estimations of the equilibrium charge state, 16.8+ and 12.7+, we thus have the equilibration length falling in the interval 3.0–6.7 nm and the equilibration time in 0.4–0.9 fs. Figure 4 shows the expected energy loss by (3) as a function of target thickness with the equilibration lengths here calculated for equilibrium charge state 12.7+ (cf. Fig. 2). The variation in stopping power is most significant for $x \lesssim d$, i.e., around the first 3 nm. Over this range, the equilibrium energy loss is approximately 55 keV, which is increased to 160 keV with initial charge state 25+. For charge states 8+ and 16+, the energy loss over the same range is 32 and 80 keV.

Table II gives a comparison of equilibration lengths and times obtained in this work and in previous studies. The data may be used as a starting point for generating a model of the scaling of the equilibration time with experimental parameters. It has been noted in [15] that d increases with increasing $|q_{in} - q_{eq}|$, indicating that the model proposed via (1) is not valid over large ranges of charge states without including

TABLE II. Comparison of equilibration lengths and times with values extracted from different studies. Values given in other formats for example in Table I of [35] are recalculated to equilibration length d as defined in this work. The equilibrium charge state is given according to measured value from reference if applicable, otherwise by the formula for solid state target in [26]; slightly different numbers, based on different models, are given in the references. Thicknesses of C have, where applicable, been translated from $\mu g/cm^2$ to nm using the standard bulk density of graphite.

Ion	Energy (eV)	q_{in} (X+)	q_{eq} (X+)	Target	Estimated d (nm)	t_{eq} (fs)	Ref.
^{132}Xe[a]	$1 \times 10^4 - 2.6 \times 10^5$	20	0.08–1.2[b]	graphene	not applicable	1.4–1.9	[37,38]
		24–25		graphene		1.3–2.4	[37,38]
		30		graphene		1.8–3.8	[37,38]
		32		graphene		1.8	[37]
		35		graphene		2.2	[37]
		20		MoS$_2$		2.0	[38]
		24		MoS$_2$		2.3	[38]
		30		MoS$_2$		3.1	[38]
^{84}Kr[a]	2.0×10^5	33	1.1[b]	C	≈ 0.7	≈ 1	[12]
^{197}Au	4.5×10^5	33–69	1.6[b]	C	1–4	2-6	[12]
^{132}Xe[a]	$(2.0-6.6) \times 10^5$	44	1.0–2.2[b]	C	not applicable	2.1	[39]
^{197}Au	$(3.1-9.9) \times 10^5$	68	1.2–2.7[b]	C		1.9	[39]
^{127}I	3.6×10^7	8	12.7–16.8	Au	3.0–6.0	0.4–0.8	this work
	3.6×10^7	25	12.7–16.8	Au	4.5–6.5	0.6–0.9	this work
	3.6×10^7	16	12.7	Au	6.7	0.9	this work
^{58}Ni	6.0×10^7	8	13.3	C	5.6	0.4	[25]
	6.0×10^7	18	13.3	C	3.3	0.2	[25]
^{63}Cu	6.5×10^7	9	18	C	8.8	0.6	[34]
^{12}C[a]	2.4×10^7	4.8[c]	5.6	C	13	0.6	[14]
	2.4×10^7	4.9[c]	5.6	C	13	0.7	[14]
	2.4×10^7	5.0[c]	5.6	C	13	0.7	[14]
	2.4×10^7	5.3[c]	5.6	C	16	0.8	[14]
	2.4×10^7	5.7[c]	5.6	C	9	0.5	[14]
^{32}S[a]	6.4×10^7	10–15[c]	12.6	C	≈ 25	1.3	[13]
^{84}Kr[a]	3.73×10^8	21	29	C	85	2.9	[35]
^{84}Kr[a]	4.44×10^8	23	30	C	130	3.9	[35]
^{84}Kr[a]	5.52×10^8	25	31	C	150	4.3	[35]
^{208}Pb	6.01×10^9	56	73	C	1500	20	[36]
^{132}Xe	5.79×10^9	44	51.8	C	3100	34	[15]

[a]Information on isotope not provided; the most abundant isotope has been assumed.

[b]Model applied to find equilibrium charge state not valid in given energy range; value given only for rough comparison.

[c]Initial charge state given as the average charge state measured for the thinnest target in [13,14]; equilibration length from least square fit of (1) to evolution of average charge state for increasing target thickness.

a charge state dependence in d. An equivalent statement is that the travel distance required to reduce the charge state deviation from equilibrium by a given factor increases with increasing such deviations. A similar suggestion is made in [33], where an upper limit to the equilibration length based on the excess energy loss is estimated for 576-keV Ar$^{(8-16)+}$ transmitted through C foils in a manner similar to that outlined through (1)–(5) above. It is further shown in [15] that d scales with projectile specific energy approximately as $(E/m)^{1.5}$ at high energy, or with velocity to the third power for Cu, Kr, Pb, and Xe projectiles when comparing to data from [34–36]. The dependence of the equilibration times from Table II on projectile velocity is visualized in Fig. 5 in order to check the validity of this scaling and compare it to our data.

We note that the scaling of d proposed in [15] holds for projectile velocities significantly larger than the Bohr velocity. As the velocity is decreased, however, a minimum equilibration time seems to occur for $v/v_0 \gtrsim 1$. To offer a tentative explanation for this behavior, we may return to the original definition of the equilibration length, in accordance with

Eq. (2.5) in [31],

$$d = \frac{1}{\varrho \Omega(\alpha_l - \alpha_c)}, \quad (6)$$

where Ω is the equal value for single electron capture and loss cross sections at charge state equilibrium, and ϱ is the atom density in the target. α_l and α_c are small ($|\alpha_{l,c}| \ll 1$) constants, the former positive and the latter negative, describing how the electron exchange cross sections vary when the charge state is shifted away from equilibrium:

$$\sigma_{capture} = \Omega[1 + \alpha_c(q_{eq} - q)]$$
$$\sigma_{loss} = \Omega[1 + \alpha_l(q_{eq} - q)]. \quad (7)$$

Equations (7) make it explicitly clear that the electron exchange cross sections are crucial for determining the equilibration length. Especially at high velocities, where the majority of existing data are for initial charge states below an equilibrium close to a fully stripped state, the determining parameter is the ionization cross section. The minimum
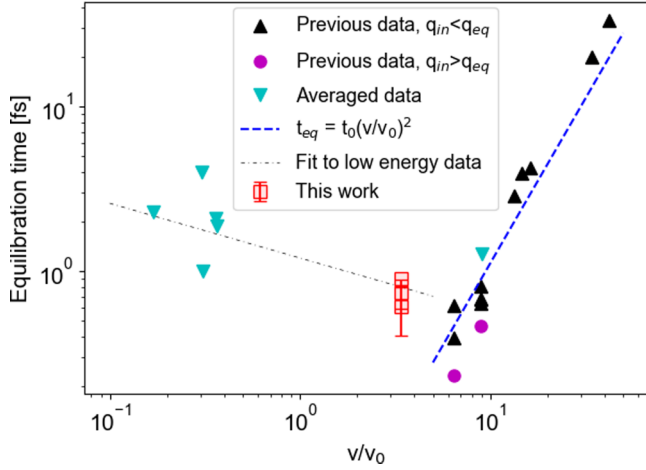
FIG. 5. Charge state equilibration time for ion-target combinations listed in Table II plotted against projectile velocity relative to the Bohr velocity v_0. Error bars on data points obtained in this work indicate the ranges of equilibration times obtained when varying the assumed equilibrium charge state from $12.7+$ as given by Bohr's simple formula [32] to $16.8+$ by the formula for solid target in [26]. The dashed blue line gives an example of v^2 scaling of t_{eq}, corresponding to the scaling of d with $(E/m)^{1.5}$ proposed in [15], while the dash-dotted thin line is a fit to the data below $5v_0$ as a guide to the eye. The points denoted by teal, downward pointing triangles have been taken as the average values based on several initial charge states and/or projectile energies from [12,13,37–39] since several charge states yield similar equilibration lengths in [13], multiple charge states are required for calculating the equilibration time in [12] and multiple projectile velocities are required for calculating the equilibration time in [37–39].

observed in t_{eq} corresponds qualitatively to the ionization cross section maximum at a projectile velocity close to the orbital velocity of the electron that is to be removed [40]. For reference, the binding energies of the $4p$ and $4d$ states (the highest populated states in ground state of $^{127}I^{16+}$ and $^{127}I^{17+}$) in unperturbed ^{127}I translate to velocities of 2–$3v_0$, while the ionization energy of 393 eV for $^{127}I^{16+}$ yields approximately $5v_0$.

At projectile velocity lower than v_0, available data in [12,37–39] treat the case of $q_{in} \gg q_{eq}$, where the time required to populate vacant high-n electron states in the projectile and subsequently de-excite the system becomes relevant. Differences between the de-excitation pathways in different highly charged ions discussed in [12] help explain that the low energy data in Fig. 5 are scattered whereas the high energy data for all projectile species are reasonably well described by a single line. The equilibration time, governed by the characteristic times for electron loss and capture, thus varies based on the dominant mechanisms by which such exchanges occur. The present data for 36-MeV ^{127}I falls in an intermediate velocity region where the $(E/m)^{1.5}$ scaling from [15] is invalid.

When assuming, as we have done in this work, that the instantaneous stopping power scales with instantaneous charge state, q, squared we may note the following. If at some depth we have a charge state distribution, $f(q)$, of ions, the effective charge state which would give rise to the average stopping

is $q_{\text{eff}} = \sqrt{\sum_q q^2 f(q)}$. This is not the same as the average charge state, $q_{\text{eq}} = \sum_q q f(q)$. In fact, the quantity $q_{\text{eff}}^2 - q_{\text{eq}}^2$ is by definition the variance of the equilibrium charge state distribution $f(q)$. Thus, the effective charge state is an overestimation of the average charge state. Similarly by measuring the average energy loss in this work, we slightly overestimate the energy loss associated with the average charge state evolution. As a result we calculate energy loss deviations and equilibration lengths that differ slightly from the real values. The calculation becomes exact if the charge state variance during equilibration is 0, i.e., at every depth all ions are in the same charge state. This is true in our case for depth 0 as the incoming charge state is unambiguously selected when looking at a single peak in the recorded ToF spectrum. Since the distribution widens over the equilibration range, however, our calculated equilibration lengths contain resulting errors. We estimate that these errors are negligible compared to our other experimental errors.

A tendency for charge states above equilibrium to equilibrate faster than those below equilibrium is indicated in Fig. 5, although the opposite is implied in Fig. 2 of [24], suggesting an asymmetry in the variation of the electron exchange cross sections with positive and negative charge state deviation. The variation of primary ion species, and the variation of target material from carbon to gold (see Table II) or even switching between different two-dimensional (2D) materials such as graphene and MoS_2 in [37,38], does not seem to have a dramatic effect on the typical equilibration lengths and times. This observation, which for slow highly charged ions is discussed extensively in [38], is in analogy to the observed similarity of the energy loss of even very slow light ions (with similar energy to mass ratio) in materials with very different electronic structure such as LiF and Au [41,42].

V. SUMMARY AND OUTLOOK

We have measured the charge-state dependent energy loss of 36-MeV ^{127}I in Au, and calculated the corresponding charge state equilibration time. Our result helps fill the existing gap between data at high ($v \gg v_0$) and low ($v \ll v_0$) energy, and provides a point above v_0 where a deviation from the high energy scaling with v^2 is obtained, to add to the data provided in [12,32,33,39]. However, our data are with a Au target, as opposed to the C target used in most experiments referenced in Table II. Thus, to verify the behavior close to v_0, further measurements with a single target material, or several measurement series with different targets, are required.

The deviation from equilibrium stopping power during charge state equilibration, as seen in Fig. 4, affects nanostructures formed during irradiation in different ways depending on whether the initial charge state is above or below the equilibrium value. For a lower-than-equilibrium initial charge state a decreased stopping power is exhibited during equilibration. A damage creation threshold [4] may thus be reached at a specific depth, giving rise to ion tracks that start below the surface and with radii that increase over the equilibration region. For initial charge states above equilibrium, tracks are expected to start at the surface and exhibit radii that decrease as the charge state equilibrates. For the effect to be most prominent,

the electronic energy loss over the equilibration region should be close to a damage creation threshold, and the equilibration length should be reasonably small in order to increase the stopping power gradient. The easiest practically achievable demonstration case using a tandem accelerator without a second stripping foil is to use charge states below equilibrium, as these become abundant when stripping occurs at the high-voltage terminal at energies typically around one or a few MeV (i.e., lower than the energy at which ions are delivered to the target). Already 36-MeV ^{127}I, as studied in this work, is relevant for investigating irradiation-induced damage since the equilibration length is near minimum and the electronic stopping power in CaF_2 (9.05 keV/nm, SRIM2013) is between the damage creation thresholds obtained in [4].

When it comes to implications for interpretation of ToF-ERDA data, we note that our energy loss offset for ^{127}I at 36 MeV corresponds to a path length in the target of about 8 nm. This will be of little importance in typical experiments, and would not significantly alter the surface depth resolution reported in [21]. As demonstrated in [22,23], however, the effect is important when monolayer resolution is attempted.

APPENDIX: EXPERIMENTAL DETAILS AND IN-DEPTH ERROR ANALYSIS

1. Au foil preparation and characterization

Au films were prepared on glass substrates by magnetron sputtering using a Balzers Union MED010 coater. Each substrate was initially cleaned with isopropanol after which a layer of NaI was evaporated onto the clean surface and an Au film was sputtered on top of that layer. Self-supporting foils were produced by dissolving the NaI layers in water and depositing the Au films across circular apertures in stainless steel (316L, 1.4404) plates. The holder on which the plates were subsequently mounted, shown in Fig. 1, is appropriately curved and was placed on a rotatable arm such that each foil could be positioned with the aperture centered in front of the ToF detector, exposed to the ion beam at normal incidence.

The foil samples were characterized by Rutherford backscattering spectrometry (RBS) using a 2-MeV ^{4}He$^+$ beam in order to obtain data on the thicknesses of the Au layers. Backscattered particles were registered with an Ortec Ultra ion implanted silicon detector at $136 \pm 2°$ backscattering angle. Following the energy loss measurements (described in further detail below), the foils were characterized with ToF-ERDA [27] using a 36-MeV ^{127}I^{8+} beam in order to determine their impurity content. The ToF-ERDA measurements were performed *ex situ*, after attempting to position the beam spot
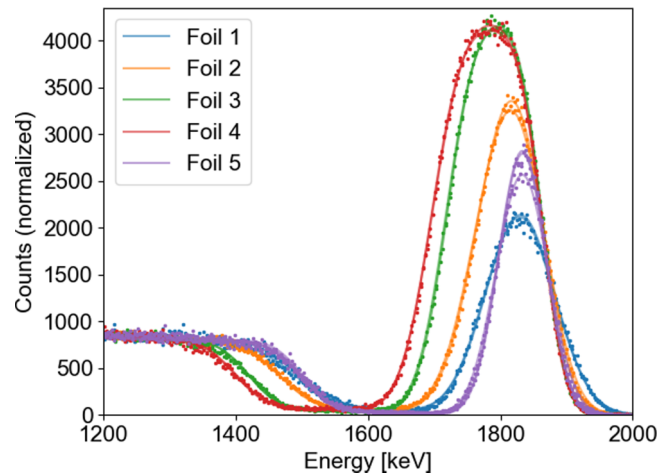

FIG. 6. RBS data (dots) and corresponding SIMNRA calculations (lines) for all measurement points on each foil.

entirely on the part of the self-supporting section of each foil covering the aperture in the steel substrate to exclude signals originating from impurities other than those present in and on the foil. The angle of the incoming beam with respect to the sample surface was $23 \pm 1°$ and recoils were detected at 45° scattering angle.

All recorded RBS spectra are shown in Fig. 6, along with SIMNRA [43] calculations yielding the total amount of Au atoms per unit area. The inconsistency in peak width is caused by electronic noise, the amplitude of which was affected by the distance between the sample holder and the backscattering detector. As such, the spectra from foil 1 and foil 5, which are of similar thickness, look qualitatively different. The substrate, which in this case is the 316L stainless steel plate on which the foils were kept, was assumed to contain all chemical elements specified in the manufacturer datasheet at a concentration corresponding to the central value of the provided tolerance range. In addition, an artificial Au fraction up to 0.6 at. % was allowed in the substrate and not counted towards the total amount of Au in the film, to reproduce the background at energies above that corresponding to the substrate Mo signal. The product of time integrated beam current to the sample and detector solid angle was adapted to reproduce the signal height at the substrate signal edge. The peak shape variation due to the changing noise amplitude was reproduced by varying the detector resolution and layer roughness, conserving the total number of counts in the peak.

The data obtained with ToF-ERDA was converted to depth profiles using Potku [44], and integrated over the film thickness to yield the composition with impurities. Signals from H, C, and O were detected and included in the analysis. The resulting atomic fractions were used as the composition of the film when fitting the RBS data in SIMNRA. Table III gives the amounts of each detected element thus found in the foils. In the rightmost column, the impurity amounts have been scaled by the ratio of SRIM electronic stopping of 36-MeV ^{127}I in the element in question to that in Au, and added to the measured amount of Au in order to yield a compensated Au foil thickness, effectively taking the impurities into account in accordance with Bragg's rule [45].

TABLE III. Areal density of elements detected in two to three points on each Au foil. The rightmost column gives the effective pure Au film thickness where contribution from impurities is taken into account in accordance with Bragg's rule. The estimated error in this number is taken as the difference between the values obtained at the different measurement points, and the given value is the average.

		10^{15} at./cm^2									
Foil	H			C			O			Au			Au$_{\text{eff}}$

Foil	H			C			O			Au			Au$_{\text{eff}}$
1	3.82	3.68		6.83	6.58		2.66	2.57		257.69	248.18		256 ± 10
2	4.13	4.11		6.42	6.39		3.51	3.49		367.94	366.01		370 ± 2
3	5.39	5.46		7.21	7.30		5.36	5.42		541.05	547.83		549 ± 7
4	4.86	4.91		7.77	7.84		4.45	4.49		622.92	628.76		630 ± 6
5[a]	3.31	3.33	3.34	5.92	5.95	5.97	2.31	2.32	2.33	223.45	224.41	225.36	227 ± 2

[a]Foil 5 broke during mounting for the ToF-ERDA measurement, and the impurity fractions could therefore not be accurately measured. The composition of the similar foil 1 has been assumed.

The foil thicknesses as measured here are noted to display relatively small differences between the different measurement points, indicating that the thickness variation along the sideways direction in Fig. 1 is similarly small. A variation of the position in the up or down direction in the figure, on the other hand, corresponds to a change of the radial position under the center of the sputter target in the system where the foils were produced. As such, a thickness variation in this direction is expected. As the foils were only movable sideways with respect to the ToF detector, we estimate that the height at which detected ions passed the foil was similar for all measurements, thus eliminating a contribution to the measured energy loss from significant variation of the foil thickness.

2. Preparation of highly charged MeV ion beam

^{127}I$^-$ ions were prepared in a Cs sputter source and accelerated to either 10 or 36 MeV using the 5-MV pelletron tandem accelerator at Uppsala University. Stripping of the ions to the desired charge states occurred in two steps. For 10-MeV ^{127}I^{3+} and ^{127}I^{8+} as well as 36-MeV ^{127}I^{8+} only the first stripping step in an Ar gas cell at the high voltage terminal of the tandem accelerator was applied. In the case of 36-MeV ^{127}I^{16+} and ^{127}I^{25+}, a 10-μg/cm^2 C foil was introduced into the beam path immediately after the accelerator. For a given charge state the energy was then selected in a double-focusing analyzing magnet with bending radius 1.270 m. When applying an additional stripping foil after the tandem accelerator (but before the analyzing magnet), each charge state produced in the terminal gas cell is accelerated to a corresponding energy and stripped to a multitude of charge states in the foil. As such, there are multiple charge-state–energy combinations that may pass the magnet with the same bending radius. Table IV lists all such combinations expected to occur when the terminal voltage and analyzing magnet field are selected in order to produce 36-MeV ^{127}I^{16+} and ^{127}I^{25+}.

3. Energy loss measurements

Ions (and neutrals) were detected at the end of the beamline in an electron mirror-type ToF-detector (EMTD) of the design described in [28] with approximately 20-cm flight path and 8-μg/cm^2 C foils in each detection unit. The following standard voltages were applied to the components of the EMTD.

C foil: -2800 V; acceleration harp and field free region: -1800 V; mirror harp: -3800 V. 800 V was applied across each microchannel plate (MCP), 100 V between the back of the first MCP and the front of the second, and 100 V between the back of the second MCP and the signal plate. The front harp shown in [28] was not used. The first amplification step after each MCP stack was a FAST ComTec TA2000B-1 preamplifier. The outputs from the preamplifiers were fed through an Ortec 935 constant fraction discriminator to an Ortec 467 time to pulse height converter, whose output was binned to produce the raw ToF spectra.

In order to calibrate the flight time measurement, data were acquired without Au foil for three charge-state–energy combinations close to the equilibrium charge state in the C foils of the ToF detector: 6-MeV ^{127}I^{5+}, 10-MeV ^{127}I^{8+}, and 36-MeV ^{127}I^{16+}. In each case Gaussian distributions were fitted to the number of counts as a function of ToF channel number in order to assign a central channel number to the ToF peak. The expected flight time over a 20-cm path was calculated by compensating the incoming ion energies by the expected stopping from SRIM2013 [29] in the first detector foil. Two spectra were acquired for each charge-state-energy combination and the average fit position was used for the calibration. The difference in peak position between the two subsequent spectra was in all three cases approximately 20 ps due to a slight drift in the signal processing electronics combined with the fit error. As the voltages on the EMTD grids were not perfectly reproduced between measurement sessions, a small calibration offset was added to make the calibration line cross exactly through the 36-MeV point when processing 36-MeV data, and similarly with the 10-MeV point for 10-MeV data. The offsets were approximately -32 ps (-85 keV for 36 MeV) and 82 ps (32 keV for 10 MeV), which may be compared to the total measured flight time of 27.16 and 51.65 ns, respectively.

For each measurement run, a spectrum was first acquired without Au foil. The Au foils were then placed in front of the detector in sequence and spectra were recorded, after which a second measurement without Au foil was performed in order to keep track of any potential drift possibly leading to a modification of the time-of-flight calibration as described above. Without Au foil, a flight time peak with standard deviation $\sigma \approx 250$ ps was measured, i.e., a FWHM slightly over 400 ps per EMTD unit. This value is close to the predicted resolution

TABLE IV. Ions expected to pass the analyzing magnet when selecting operating conditions to produce 36-MeV $^{127}I^{16+}$ (upper section) and $^{127}I^{25+}$ (lower section). Q_T: charge state after terminal; E_{acc}: approximate energy to which ions are accelerated before second stripping step (neglecting preacceleration voltage and energy loss in the terminal); Q_{mag}: charge state which enables ions to pass the analyzing magnet; E_{mag}: energy at which ions pass the analyzing magnet; $Q_{eq,Au}$: equilibrium charge state at energy E_{mag} in Au [26]. For values of Q_T other than those listed here, the energy after the second stripping step is not near a value suitable to pass the analyzing magnet for any charge state.

36-MeV $^{127}I^{16+}$: $V_{terminal} \approx 4.05$ MeV, $B_{magnet} = 4789 \pm 1.2$ G				
Q_T (X+)	E_{acc} (MeV)	Q_{mag} (X+)	E_{mag} (MeV)	$Q_{eq,Au}$ (X+)
8	36.45	16	36.00	16.8
7	32.40	15	31.64	16.0
6	28.35	14	27.56	15.2
5	24.30	13	23.77	14.3
36-MeV $^{127}I^{25+}$: $V_{terminal} \approx 4.07$ MeV, $B_{magnet} = 3065 \pm 1.2$ G				
Q_T (X+)	E_{acc} (MeV)	Q_{mag} (X+)	E_{mag} (MeV)	$Q_{eq,Au}$ (X+)
8	36.63	25	36.00	16.8
7	32.56	23	30.47	15.8
6	28.49	22	27.88	15.3
5	24.42	20	23.04	14.1
4	20.35	18	18.66	13.0
3	16.28	16	14.75	11.7
2	12.21	14	11.29	10.4

for such units as calculated in [46] with acceleration potential of 1 kV, and in accordance with the value stated in [28]. With $\Delta E/E = 2\Delta t/t$, the resulting peak FWHM in energy is approximately 230 keV at $E = 10$ MeV and 1.6 MeV at $E = 36$ MeV (see also Figs. 7 and 8), however by fitting the peaks with Gaussians their position may be determined to better accuracy. The recorded flight time spectra were calibrated and energy-converted to yield the ion energy after the first EMTD foil. A compensation was performed for energy loss in the EMTD foil using SRIM2013 stopping in C at the measured energy. The spectra thus produced are marked below as "energy before detector."

Figure 7 gives an example of energy spectra obtained for 10-MeV $^{127}I^{8+}$ with each Au foil. In addition to the peak a few
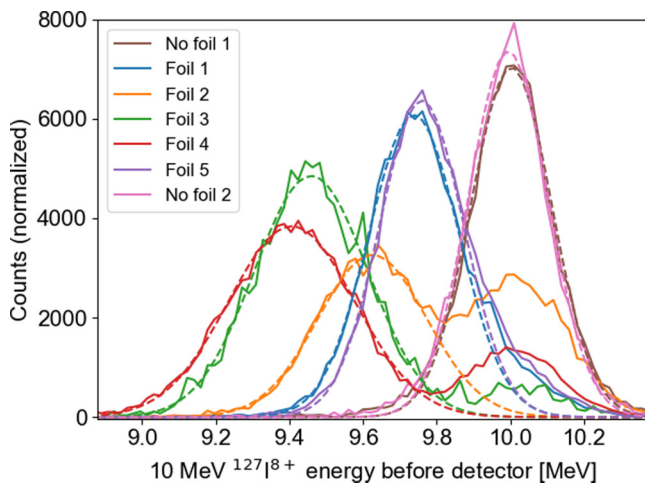

FIG. 7. Energy converted ToF spectra for 10-MeV $^{127}I^{8+}$ with and without Au foils, compensated for energy loss in the first EMTD foil. Solid lines represent data while dashed lines are Gaussian distributions fit to the channel range of interest for each peak.

hundred keV below that obtained without foil, there is also a peak for each foil where no energy loss has occurred. This peak is due to ions passing through small tears or pinholes. Even though the total pinhole area is small in comparison to the area of the foil, the reduction of the signal intensity due to scattering of the ions that pass through the foil makes the pinhole-related peak relatively large. Gaussian distributions have been fit to the peak at lower energy, and the energy loss in the Au foil in each case is taken as the difference between the energy selected in the analyzing magnet and the peak position from the fit. In order to minimize the effect of the pinhole-peak on the obtained energy loss, the channel ranges over which these fits were performed have been selected manually to cover the low energy side of the peak, up until approximately 100 keV above the position of the maximum. The peaks recorded without Au foil were fit over their full width, yielding an energy loss without foil which if nonzero indicates a measurable charge state dependent energy loss in the first EMTD foil.

Data obtained for 36-MeV $^{127}I^{16+}$ and $^{127}I^{25+}$ are visualized in Figs. 8(a) and 8(b). All expected charge-state–energy pairs as listed in Table IV are detected. The relative signal intensities for different charge states depend both on the charge state distribution after the stripping foil [47], and how far from the center of the energy distribution after stripping the appropriate energy given in Table IV is. This explains, for example, the larger height of the peak associated with initial charge state 13+ compared to those for 14+ and 15+ in Fig. 8(a). The pinhole-related peaks seen in Fig. 7 are more difficult to detect in this case for two reasons. First, while the energy loss at higher energy is larger, the worsening of the energy resolution more than compensates so that the peaks end up overlapping to a larger degree at 36 MeV than at 10 MeV. The second reason is that with increasing energy, a smaller fraction of ions are scattered to such a large angle that they miss the ToF detector, significantly reducing the relative height of the peak
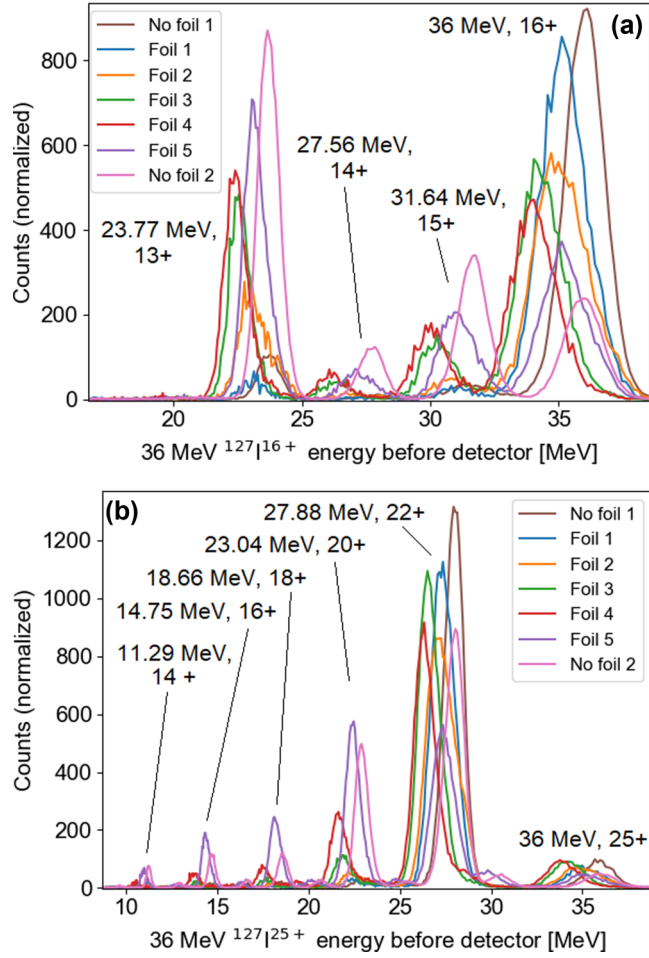
FIG. 8. Ions reaching the Au foil (or ToF detector) in configuration selected to produce (a) 36-MeV $^{127}I^{16+}$: $V_{\text{terminal}} \approx 4.05$ MV, $B_{\text{magnet}} = 4789 \pm 1.2$ G; (b) 36-MeV $^{127}I^{25+}$: $V_{\text{terminal}} \approx 4.07$ MV, $B_{\text{magnet}} = 3065 \pm 1.2$ G. Spectra were recorded once with each Au foil present, and twice without foil.

originating from pinholes. In any case, the method of fitting Gaussian distributions to the low energy-side and maximum of the peak was also used for these data. Care was taken when selecting fit ranges for the peaks associated with initial ion energy 36 MeV to not include any contribution from nearby peaks for different charge-state–energy combinations.

The data obtained with Au foils 3–5 as well as the second run without foil were estimated to contain enough counts to fit the peak positions in the peak groups associated with energies lower than 36 MeV in Fig. 8. In the case of Fig. 8(a), also the data with Au foil 2 was considered. Since the ToF calibration offset in these cases was selected to minimize the error at 36 MeV, it was assumed that a small deviation would occur at other energies. As such, the energy losses shown in Fig. 3 were measured as the difference in peak position with and without Au foil, rather than the difference between the measured peak position and the energy selected in the analyzing magnet (which was the case for Fig. 2).

A comparison between spectra obtained with three of the Au foils as well as one measurement without foil and three different initial charge states at 36 MeV is shown in Fig. 9
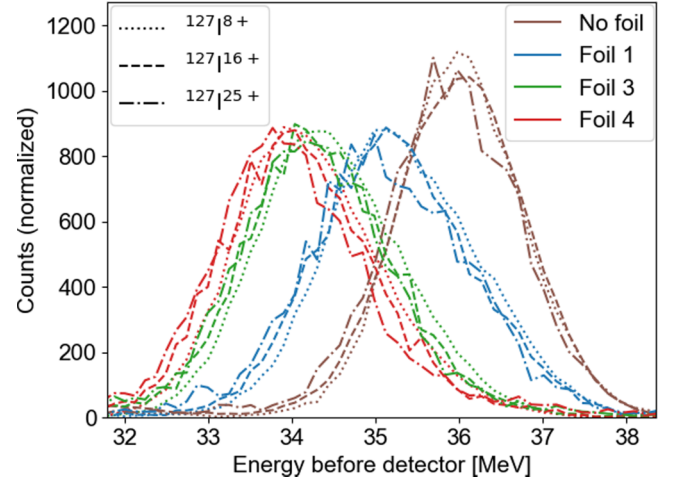

FIG. 9. Energy converted ToF spectra obtained for primary ^{127}I ion energy 36 MeV with three different initial charge states and three different Au foils, as well as a measurement without foil.

to illustrate the effect of charge state dependent stopping. A shift of the peak towards the left is noted as the charge state is increased, indicating an increased energy loss. A smaller shift is noted also for the measurement without foil, which is expected due to charge state dependent stopping in the first EMTD foil in that case.

4. In-depth experimental error analysis

In order to assess whether the drifts noted between the runs with and without Au foils have an impact on our conclusions, we may start by noting that the typical ± 20-ps drift corresponds to 53 keV in the 36-MeV case and 7.7 keV for 10 MeV. As such, the drift is large enough to potentially affect even the qualitative interpretation of data in an unfortunate case. In order to mitigate this potential error source, the data at 36 MeV for charge state 16+ was acquired first, then 25+, and last 8+. As such, any systematic drift which could potentially have given rise to the measured effect would have caused an opposite than expected offset either for charge state 8+ or 25+. Further, as seen from Figs. 2 and 9, the measured offset is consistent for each foil, which would be an unlikely outcome in the case of significant drift contribution. When it comes to the ToF calibration offsets, these only introduce a difference between the dataset obtained at 10 MeV on the one hand, and that obtained at 36 MeV on the other. As such, they have no effect on the measured energy loss offsets for 36 MeV. We may further note that the charge states used for the ToF calibration at 6 and 10 MeV are below the equilibrium values calculated from the formula for a solid target in [26], but this is of no consequence as the charge state dependent stopping at those energies with initial state reasonably close to the equilibrium is small in this study (as explicitly shown in Fig. 2).

The field in the analyzing magnet, by which the ion energy was selected, was measured independently with two instruments; a Hall probe and a nuclear magnetic resonance (NMR) probe separated by approximately 8 cm. The measured values differed due to field inhomogeneity, giving rise to an offset

that scaled with B as $\Delta B/B \approx 3.7 \times 10^{-4}$. This number is indicative of the misrepresentation of the average field in the magnet due to inhomogeneity. With $\Delta E/E = 2\Delta B/B$, the associated errors in energy for a given energy are the same for all charge states and do not affect our measured energy loss offsets. A more important error in the magnetic field for the present work is a constant offset of $\Delta B \approx 1.2$ G that occurs due to hysteresis between the cases where a selected field strength is approached from lower or higher values. As the field is regulated in one point (on either probe), the offset due to this hysteresis effect gives a different misrepresentation in cases of increasing and decreasing field. Assuming that the magnetic field error is the measured 1.2 G, the corresponding errors in energy are 28 keV for 36-MeV $^{127}I^{25+}$, 18 keV for 16+, and 9 keV for 8+. At 10 MeV we have 5 keV for charge state 8+ and 2 keV for 3+. Due to the order in which our measurements were performed, charge state 16+ at 36 MeV was measured at increasing field, 25+ at decreasing field, and 8+ at increasing field. Similarly to the note on drifts above, a systematic error due to magnetic field hysteresis could thus affect the data obtained for 25+, but it cannot explain the offset between charge states 8+ and 16+. Furthermore, the offset between data obtained with charge states 16+ and 25+, as shown in Fig. 2, is larger with Au foil present than without which is consistent with what one would expect for charge state dependent stopping and inconsistent with an offset caused by magnetic field hysteresis. Nevertheless, the errors here given for $\Delta B = 1.2$ G are included in the error bars in Fig. 2. Combining the errors so far discussed, especially drift and magnetic field uncertainty, we estimate that our measured energy loss offsets carry errors on the order of at least 30%.

A further potential error source is uncertainties in the distance over which the flight time is measured and the thickness of the first EMTD foil, for which the measured energy is compensated. As the ToF calibration is performed assuming a distance of 20 cm, however, the calibrated data give the flight time of ions over 20 cm, regardless of the actual flight distance, and thus yield a correct energy (i.e., the flight distance is calibrated out). For the first EMTD foil, the assumed thickness used for the calibration is the same as the thickness used for compensating the measured energy. Over the range of energies shown in Fig. 9, the equilibrium electronic stopping power of ^{127}I in C varies between approximately 38 and 41 keV/($\mu g/cm^2$). An error in the foil thickness of, say, $5\,\mu g/cm^2$ (63%) would therefore yield an error in the energy loss compensation that differed by approximately 15 keV over the depicted energy range. For each foil, the error would be significantly smaller, not contributing in a manner relevant to our conclusions.

There are several factors contributing to the fact that we obtain a measurable charge state-dependent energy loss at 36 MeV but not at 10 MeV. The equilibrium stopping powers differ by more than a factor 3, which carries over to the expected offset [see Eq. (5)]. Further, assuming the same equilibration time, the equilibration path length in the 10-MeV case is shorter by a factor close to 2. The offset should therefore be maximally 1/6 of that obtained at 36 MeV for a similar charge state ratio, or in our case around 20 keV. Judging by the calculated energy losses in Fig. 4 we may expect a larger deviation for charge states above equilibrium than for those below. Since neither charge state applied at 10 MeV is far above equilibrium, we estimate that the offset in that case is not resolvable in our setup.

A seemingly peculiar feature of Fig. 8 is that it seems like the relative amounts of different charge states hitting the detector vary over time, in particular between the first and second measurement without Au foil. This is explained by a continuous deterioration of the stripping C foil over the course of the measurements. As the amount of material in the beam path changed, so did the charge state distribution. In Fig. 8(b), small peaks related to charge states 15+, 17+, 19+, and 21+ can be noticed between the expected ones. These are caused by ions on the tails of the energy distributions after the second stripping foil, but contain too few counts for any analysis to be performed.

[1] M. Nastasi, J. W. Mayer, and J. K. Hirvonen, Ion stopping, in *Ion-Solid Interactions, Fundamentals and Applications*, edited by D. R. Clarke, S. Suresh, and I. M. Ward (Cambridge University Press, Cambridge, UK, 1996), pp. 88–114.

[2] G. Foti, J. W. Mayer, and E. Rimini, Backscattering Spectrometry, in *Ion Beam Handbook for Material Analysis*, edited by J. W. Mayer and E. Rimini (Academic Press, New York, 1977), pp. 21–65.

[3] M. Backman, F. Djurabekova, O. H. Pakarinen, K. Nordlund, Y. Zhang, M. Toulemonde, and W. J. Weber, Cooperative effect of electronic and nuclear stopping on ion irradiation damage in silica, J. Phys. D: Appl. Phys. **45**, 505305 (2012).

[4] M. Toulemonde, A. Benyagoub, C. Trautmann, N. Khalfaoui, M. Boccanfuso, C. Dufour, F. Gourbilleau, J. J. Grob, J. P. Stoquert, J. M. Costantini, F. Haas, E. Jacquet, K.-O. Voss, and A. Meftah, Dense and nanometric electronic excitations induced by swift heavy ions in an ionic CaF2 crystal: Evidence for two thresholds of damage creation, Phys. Rev. B **85**, 054112 (2012).

[5] A. Arnau, M. Peñalba, P.M. Echenique, and F. Flores, A charge state approach to the stopping of ions in solids, Nucl. Instrum. Methods Phys. Res. B **69**, 102 (1992).

[6] P. Sigmund, Stopping of Swift Point Charge I: Bohr and Bethe Theory, in *Particle Penetration and Radiation Effects*, Springer Series in Solid-state Sciences Vol. 151, edited by M. Cardona, P. Fulde, K. von Klitzing, R. Merlin, H.-J. Queisser, and H. Störmer (Springer-Verlag, Berlin, 2006), pp. 109–139.

[7] J. M. Anthony and W. A. Lanford, Stopping power and effective charge of heavy ions in solids, Phys. Rev. A **25**, 1868 (1982).

[8] Y.-L. Fu, Z.-J. Zhang, C.-K Li, H.-B Sang, W. Cheng, and F.-S Zhang, Electronic stopping power for slow ions in the low-hardness semimetal HgTe using first-principles calculations, J. Phys.: Condens. Matter **32**, 105701 (2020).

[9] S. Lohmann and D. Primetzhofer, Disparate Energy Scaling of Trajectory-Dependent Electronic Excitations for Slow Protons and He Ions, Phys. Rev. Lett. **124**, 096601 (2020).

[10] J. I. Juaristi, A. Arnau, P. M. Echenique, C. Auth, and H. Winter, Charge State Dependence of the Energy Loss of Slow Ions in Metals, Phys. Rev. Lett. **82**, 1048 (1999).

[11] Y. Mu, A. Burenkov, H. Ryssel, Y. Xia, and L. Mei, Charge-state dependence of stopping power for light ions penetrating thin carbon foils at low velocity, Nucl. Instrum. Methods Phys. Res. B **164–165**, 272 (2000).

[12] T. Schenkel, M. A. Briere, A. V. Barnes, A. V. Hamza, K. Bethge, H. Schmidt-Böcking, and D. H. Schneider, Charge State Dependent Energy Loss of Slow Heavy Ions in Solids, Phys. Rev. Lett. **79**, 2030 (1997).

[13] M. Imai, M. Sataka, K. Kawatsura, K. Takahiro, K. Komaki, H. Shibata, H. Sugai, and K. Nishio, Equilibrium and non-equilibrium charge-state distributions of 2 MeV/u sulfur ions passing through carbon foils, Nucl. Instrum. Methods Phys. Res. B **267**, 2675 (2009).

[14] M. Imai, M. Sataka, M. Matsuda, S. Okayasu, K. Kawatsura, K. Takahiro, K. Komaki, H. Shibata, and K. Nishio, Equilibrium and non-equilibrium charge-state distributions of 2.0 MeV/u carbon ions passing through carbon foils, Nucl. Instrum. Methods Phys. Res. B **354**, 172 (2015).

[15] M. Toulemonde, Irradiation by swift heavy ions: Influence of the non-equilibrium projectile charge state for near surface experiments, Nucl. Instrum. Methods Phys. Res. B **250**, 263 (2006).

[16] S. Facsko, R. Heller, A. S. El-Said, W. Meissl, and F. Aumayr, Surface nanostructures by single highly charged ions, J. Phys.: Condens. Matter **21**, 224012 (2009).

[17] M. Toulemonde, C. Trautmann, E. Balanzat, K. Hjort, and A. Weidinger, Track formation and fabrication of nanostructures with MeV-ion beams, Nucl. Instrum. Methods Phys. Res. B **216**, 1 (2004).

[18] A. S. El-Said, R. A. Wilhelm, R. Heller, S. Facsko, C. Lemell, G. Wachter, J. Burgdörfer, R. Ritter, and F. Aumayr, Phase Diagram for Nanostructuring CaF2 Surfaces by Slow Highly Charged Ions, Phys. Rev. Lett. **109**, 117602 (2012).

[19] Z. Siwy, P. Apel, D. Baur, D. D. Dobrev, Y. E. Korchev, R. Neumann, R. Spohr, C. Trautmann, and K.-O. Voss, Preparation of synthetic nanopores with transport properties analogous to biological channels, Surf. Sci. **532–535**, 1061 (2003).

[20] I. Vlassiouk, P. Y. Apel, S. N. Dmitriev, K. Healy, and Z. S. Siwy, Versatile ultrathin nanoporous silicon nitride membranes, Proc. Natl. Acad. Sci. U.S.A. **106**, 21039 (2009).

[21] Z. Siketić, I. Bogdanović Radović, I. Sudić, and M. Jakšić, Surface analysis and depth profiling using time-of-flight elastic recoil detection analysis with argon sputtering, Sci. Rep. **8**, 10392 (2018).

[22] G. Dollinger, C. M. Frey, A. Bergmaier, and T. Faestermann, Elastic recoil detection with single atomic layer depth resolution, Nucl. Instrum. Methods Phys. Res. B **136–138**, 603 (1998).

[23] G. Dollinger, C. M. Frey, A. Bergmaier, and T. Faestermann, Depth profile analysis with monolayer resolution using elastic recoil detection (ERD), Europhys. Lett. **42**, 25 (1998).

[24] C. M. Frey, G. Dollinger, A. Bergmaier, T. Faestermann, and P. Maier-Komor, Charge state dependence of the stopping power of 1 MeV/A 58Ni-ions in thin carbon foils, Nucl. Instrum. Methods Phys. Res. B **99**, 205 (1995).

[25] C. M. Frey, G. Dollinger, A. Bergmaier, T. Faestermann, and P. Maier-Komor, Charge state dependence of the stopping power of 1 MeV/A 58Ni ions, Nucl. Instrum. Methods Phys. Res. B **107**, 31 (1996).

[26] G. Schiwietz and P. L. Grande, Improved charge-state formulas, Nucl. Instrum. Methods Phys. Res. B **175–177**, 125 (2001).

[27] P. Ström, P. Petersson, M. Rubel, and G. Possnert, A combined segmented anode gas ionization chamber and time-of-flight detector for heavy ion elastic recoil detection analysis, Rev. Sci. Instrum. **87**, 103303 (2016).

[28] A. V. Kuznetsov, E. J. van Veldhuizen, L. Westerberg, V. G. Lyapin, K. Aleklett, W. Loveland, J. Bondorf, B. Jakobsson, H. J. Whitlow, and M. El Bouanani, A compact Ultra-High Vacuum (UHV) compatible instrument for time of flight-energy measurements of slow heavy reaction products, Nucl. Instrum. Methods Phys. Res. A **452**, 525 (2000).

[29] J. F. Ziegler, M. D. Ziegler, and J. P. Biersack, SRIM—The stopping and range of ions in matter (2010), Nucl. Instrum. Methods Phys. Res. B **268**, 1818 (2010).

[30] K. Kantre, V. Paneta, and D. Primetzhofer, Investigation of the energy loss of I in Au at energies below the Bragg peak, Nucl. Instrum. Methods Phys. Res. B **450**, 37 (2019).

[31] N. Bohr and J. Lindhard, Electron capture and loss by heavy ions penetrating through matter, Niels Bohr Collected Works **8**, 593 (1987); Original publication in: Mat. Fys. Medd. K. Dan. Vidensk. Selsk. **28**, (1954).

[32] N. Bohr, The penetration of atomic particles through matter, Niels Bohr Collected Works **8**, 423 (1987); Original publication in: Mat. Fys. Medd. K. Dan. Vidensk. Selsk. **18**, (1948).

[33] R. Herrmann, C. L. Cocke, J. Ullrich, S. Hagmann, M. Stoeckli, and H. Schmidt-Boecking, Charge-state equilibration length of a highly charged ion inside a carbon solid, Phys. Rev. A **50**, 1435 (1994).

[34] K. Shima, T. Ishihara, T. Miyoshi, and T. Mikumo, Equilibrium charge-state distributions of 35–146-MeV Cu ions behind carbon foils, Phys. Rev. A **28**, 2162 (1983).

[35] E. Baron and B. Delaunay, Stripping of high-energy krypton ions by various solid materials, Phys. Rev. A **12**, 40 (1975).

[36] A. Leon, S. Melki, D. Lisfi, J. P. Grandin, P. Jardin, M. G. Suraud, and A. Cassimi, Charge state distributions of swift heavy ions behind various solid targets (36 ⩽ Zp ⩽ 92, 18 MeV/u ⩽ E ⩽ 44 MeV/u), At. Data Nucl. Data Tables **69**, 217 (1998).

[37] R. A. Wilhelm, E. Gruber, J. Schwestka, R. Kozubek, T. I. Madeira, J. P. Marques, J. Kobus, A. V. Krasheninnikov, M. Schleberger, and F. Aumayr, Interatomic Coulombic Decay: the Mechanism for Rapid Deexcitation of Hollow Atoms, Phys. Rev. Lett. **119**, 103401 (2017).

[38] S. Creutzburg, J. Schwestka, A. Niggas, H. Inani, M. Tripathi, A. George, R. Heller, R. Kozubek, L. Madauß, N. McEvoy, S. Facsko, J. Kotakoski, M. Schleberger, A. Turchanin, P. L. Grande, F. Aumayr, and R. A. Wilhelm, Vanishing influence of the band gap on the charge exchange of slow highly charged ions in freestanding single-layer MoS2, Phys. Rev. B **102**, 045408 (2020).

[39] M. Hattass, T. Schenkel, A. V. Hamza, A. V. Barnes, M. W. Newman, J. W. McDonald, T. R. Niedermayr, G. A. Machicoane, and D. H. Schneider, Charge Equilibration Time of Slow, Highly Charged Ions in Solids, Phys. Rev. Lett. **82**, 4795 (1999).

[40] I. D. Kaganovich, E. Startsev, and R. C. Davidson, Scaling and formulary of cross-sections for ion–atom impact ionization, New J. Phys. **8**, 278 (2006).

[41] S. N. Markin, D. Primetzhofer, S. Prusa, M. Brunmayr, G. Kowarik, F. Aumayr, and P. Bauer, Electronic interaction of very slow light ions in Au: Electronic stopping and electron emission, Phys. Rev. B **78**, 195122 (2008).

[42] S. N. Markin, D. Primetzhofer, and P. Bauer, Vanishing Electronic Energy Loss of Very Slow Light Ions in Insulators with Large Band Gaps, Phys. Rev. Lett. **103**, 113201 (2009).

[43] M. Mayer, SIMNRA User's Guide, Report IPP 9/113, Max-Planck-Institut für Plasmaphysik, Garching, Germany, 1997.

[44] K. Arstila, J. Julin, M. I. Laitinen, J. Aalto, T. Konu, S. Kärkkäinen, S. Rahkonen, M. Raunio, J. Itkonen, J.-P. Santanen, T. Tuovinen, and T. Sajavaara, Potku–New analysis software for heavy ion elastic recoil detection analysis, Nucl. Instrum. Methods Phys. Res. B **331**, 34 (2014).

[45] W. H. Bragg and R. Kleeman, On the α particles of radium, and their loss of range in passing through various atoms and molecules, The London, Edinburgh, Dublin Philos. Mag. and J. Sci. **10**, 318 (1905).

[46] H. J. Whitlow, P. Jeanneret, E. Guibert, L. Wang, and M. Van Der Meer, Time detector design for Time-of-Flight Elastic Recoil Detection Analysis (ToF-E ERDA), Nucl. Instrum. Methods Phys. Res. B **450**, 385 (2019).

[47] V. S. Nikolaev and I. S. Dmitriev, On the equilibrium charge distribution in heavy element ion beams, Phys. Lett. A **28**, 277 (1968).